Propagation properties of the electron circular vortex beam based on the butterfly catastrophe

Hailong Wu,[1] Zhengheng Li,[2] Huilin Tang,[1] Zhejue Fan,[1] Xuezhen Cai,[1] Zien Feng,[1] Junxi Zhang,[1] Zhenhang Xu,[1] Zhang Ruan,[1] and Dongmei Deng[1,*]

[1]*Guangdong Provincial Key Laboratory of Nanophotonic Functional Materials and Devices, Guangdong Basic Research Center of Excellence for Structure and Fundamental Interactions of Matter, School of Information and Optoelectronic Science and Engineering, South China Normal University, Guangzhou 510006, China*

[2]*Faculty of Arts and Sciences, Beijing Normal University, Zhuhai 519087, China*

(Received 18 February 2024; accepted 3 May 2024; published 24 May 2024)

In this paper, an alternative kind of electron circle butterfly vortex beam (ECBVB) based on the butterfly catastrophe is introduced, and its propagation characteristics in free space and constant magnetic field are numerically discussed. In free space, the ECBVB exhibits autofocusing and self-healing properties, and the probability flow density vector and cross-section intensity distribution are also analyzed. Compared to that in the free space, the focusing intensity of the ECBVB in the magnetic field increases by two orders of magnitude. By changing the distribution factor, the magnetic flux density, and the second-order chirp factor, the autofocusing properties of the ECBVB can be adjusted flexibly. In addition, adjusting the topological charges and the initial transverse velocity of the ECBVB is conducive to obtaining the desired propagation behavior of the ECBVB.

DOI: 10.1103/PhysRevA.109.053318

I. INTRODUCTION

According to the. de Broglie theory and Born theory of quantum mechanics [1], an electron beam can be viewed as a matter wave, whose behavior can be described as a complex-valued wave function conforming to the Schrödinger equation [2]. The wave function describes the space-time probability distribution of the electron beams, linking the properties of the wave and the particle.

Inspired by structured beams [3], structured wave packets have found fertile ground in the field of electronics. A common way to customize electron-beam packets is to sculpt the electron wave function using nanoscale phase masks [4]. In 2007, the dynamics of electron wave-packet states with vortex are proposed [5]. In 2010, an electron vortex beam with helical wavefront structure was generated in experiment [6–8], and since then the theory of the electron vortex beam has been greatly improved and developed [9–12]. In 2013, Voloch-Bloch *et al.* experimentally generated a self-accelerating electron Airy beam for the first time and investigated its properties; their work proposes an alternative field for manipulating trajectories of particles by designing initial probability density wave functions of particles [13]. Then Karlovets and coworkers perfected the development of electron Airy beams in free space [14–16]. In 2014, a holographic approach was used to generate electron Bessel beams in transmission electron microscopy, and its properties such as nondiffraction and self-healing have aroused much interest [17–19]. Due to the special effect of magnetic fields on charged particles, the electron beam will rotate with constant radius and constant angular frequency in a constant magnetic field [20,21], and this unique property has been noticed by some scholars. In 2021, Goutsoulas and Efremidis investigated the dynamics of self-accelerating electron Airy beams in a constant magnetic field [22]. Subsequently, the properties of electron Pearcey and Airy wave packets in a constant magnetic field were also explored [23–25]. From the above, the various properties of the electron beams are conducive to practical applications such as high-resolution phase contrast imaging, measurement of crystal chirality, and manipulation of nanoparticles [11,26–28].

In recent years, the catastrophe theory, which shows some excellent properties, has been widely used in electron optics and electron beams with catastrophe functions [29–31]. From the perspective of the potential function, a mutation function can be divided into seven basic catastrophes: fold, cusp, swallowtail, butterfly, elliptical umbilic, hyperbolic umbilic, and parabolic umbilic. For example, the electron Airy beams described by the Airy function have the properties of self-healing and self-accelerating, corresponding to the fold catastrophe. The electron Pearcey beam described by the Pearcey function corresponds to the cusp catastrophe, which has the properties of autofocusing, self-healing, and form invariance. Until now, some higher-order catastrophes such as the swallowtail catastrophe and butterfly catastrophe have been applied in optics and proved to have some excellent properties [32,33]. However, these higher-order catastrophes have not been studied for electron beams. To fill this gap, this paper focuses on an alternative type of electron beam which is described by butterfly catastrophe, the electron circular butterfly vortex beam (ECBVB). We investigate the propagation of the ECBVB in free space and a constant magnetic field. The focal length and the focal intensity of the ECBVB not only exhibited flexible tunability but also showed different propagation properties in different environments. In the free space, the ECBVB can form an electronic bottle (EB) after adding the Gaussian absorption obstacle. In the constant magnetic

*dengdongmei@m.scnu.edu.cn

 ©2024 American Physical Society

field, its focal intensity can be two orders of magnitude higher than that in free space but the ECBVB loses self-healing property. Whether in free space or a constant magnetic field, the ECBVB exhibits the dynamic property of rotation. Moreover, we also introduce a second-order chirp factor to expand the autofocusing properties of the ECBVB further and realize the regulation of autofocusing.

II. THEORETICAL MODEL OF THE ECBVB

A. Propagation of the ECBVB in free space and constant magnetic field

In the presence of an electromagnetic field, an electron wave packet arises as a solution to the Schrödinger equation

$$\left[i\hbar\frac{\partial}{\partial t}+e\phi(\mathbf{r},t)\right]\Psi=\frac{1}{2m}\left(\hat{\boldsymbol{p}}+\frac{e}{c}\mathbf{A}\right)^2\Psi, \tag{1}$$

where $\hbar$ is the reduced Planck constant, m is the electron mass, e is the electron charge, $\hat{\boldsymbol{p}}=-i\hbar\nabla$ is the momentum operator, ϕ and $\mathbf{A}$ are respectively the scalar and the vector potentials, and Ψ is the wave function. The magnetic-field direction is aligned with the propagation z direction. The relationship between the magnetic field and vector potential is satisfied by $\mathbf{B}=\nabla\times\mathbf{A}=B\mathbf{e_z}$, and the symmetric gauge $\mathbf{A}=\frac{B}{2}(x\mathbf{e_y}-y\mathbf{e_x})$. B is the magnetic flux density. The potential function $\phi(\mathbf{r},t)=0$. The wave packet can be expressed as

$$\Psi=\psi e^{i(p_0z-E_0t)/\hbar}, \tag{2}$$

where $E_0=p_0^2/(2m)$. We define a coordinate system that moves along with the electron wave packet, $\zeta=z-\hbar k_0t/m, \tau=t$. To simplify the calculation, we use normalized dimensionless coordinates: $z\to z_0z, t\to t_0t, (x,y)\to L(x,y), B\to B_0B$, with $t_0=mL^2/\hbar, z_0=k_0L^2, B_0=c\hbar/(eL^2), p_0=\hbar k_0$. Under the paraxial approximation, we obtain

$$i\partial_\tau\psi=\left[-\frac{1}{2}\nabla_\perp^2-i\frac{B}{2}(x\partial_y-y\partial_x)+\frac{B^2}{8}(x^2+y^2)\right]\psi. \tag{3}$$

In polar coordinates, Eq. (3) can be expressed as

$$i\partial_\tau\psi=\left\{-\frac{1}{2}\left[\frac{1}{r}\frac{\partial}{\partial r}\left(r\frac{\partial}{\partial r}\right)+\frac{1}{r^2}\frac{\partial^2}{\partial\theta^2}\right]-i\frac{B}{2}\left(\frac{\partial}{\partial\theta}\right)+\frac{B^2}{8}r^2\right\}\psi. \tag{4}$$

In a constant magnetic field, the integral form of Eq. (4) can be expressed as

$$\psi(\boldsymbol{r},\tau)=\iint\psi_0(\boldsymbol{\rho})K(\boldsymbol{r},\boldsymbol{\rho},\tau)\rho d\rho d\sigma, \tag{5}$$

where $\boldsymbol{r}=x\boldsymbol{e_x}+y\boldsymbol{e_y}$, $\boldsymbol{\rho}=x'\boldsymbol{e_x}+y'\boldsymbol{e_y}$, and $\psi_0(\boldsymbol{\rho})$ is the initial wave function of the electron beam. K is the propagator of the electron beam in a longitudinal constant magnetic field, corresponding to Eq. (3). It can be written as

$$K(\boldsymbol{r},\boldsymbol{\rho},\tau)=\frac{B}{4\pi i\sin\frac{B\tau}{2}}e^{i\frac{B}{4}\cot\frac{B\tau}{2}(\boldsymbol{r}-\boldsymbol{\rho})^2+i\frac{B}{2}\boldsymbol{r}\times\boldsymbol{\rho}}. \tag{6}$$

By expanding the vector identity and combining the above formulas, we get a final expression that is easier to compute:

$$\psi=\frac{w}{2\pi i}\iint_{\mathrm{R}^2}\psi_0(\rho,\sigma)e^{iv\rho^2-i[S_1\rho\cos(\sigma)+S_2\rho\sin(\sigma)]}\rho d\rho d\sigma, \tag{7}$$

where $v=\frac{B}{4}\cot(\frac{B\tau}{2})$, $w=\frac{B}{2}\csc(\frac{B\tau}{2})e^{ivr^2}$, $S_1=2v[r\cos(\theta)+r\sin(\theta)\tan(\frac{B\tau}{2})]$, and $S_2=2v[r\sin(\theta)-r\cos(\theta)\tan(\frac{B\tau}{2})]$. According to the catastrophe theory, we know that the catastrophe function can be classified into the following seven categories: fold, cusp, swallowtail, butterfly, hyperbolic umbilic, elliptic umbilic, and parabolic umbilic catastrophes, which conform to the equation

$$C_n(a_1,a_2,\ldots,a_{n-2})=\int_{-\infty}^{\infty}\exp\{iP_n[(a_1,a_2,\ldots,a_{n-2}),s]\}ds. \tag{8}$$

The expression of the canonical potential function $P_n[(a_1,a_2,\ldots,a_{n-2}),s]$ is given by

$$P_n[(a_1,a_2,\ldots,a_{n-2}),s]=s^n+\sum_{j=1}^{n-2}a_js^j. \tag{9}$$

The butterfly function (Bu) corresponds to the case of $n=6$, and we substitute it into Eq. (8) to get the following form:

$$\mathrm{Bu}(a_1,a_2,a_3,a_4)=\int_{-\infty}^{\infty}\exp[i(s^6+a_4s^4+a_3s^3+a_2s^2+a_1s)]ds. \tag{10}$$

The butterfly catastrophe provides four control parameters that we can arbitrarily choose to use as the cross-sectional spatial coordinates. The initial wave function of the ECBVB can be expressed as

$$\psi_0(r,\theta)=A_0\mathrm{Bu}\left(0,q\frac{r_0-r}{w_0},0,0\right)\exp\left[-\left(a\frac{r_0-r}{w_0}\right)^2\right]\times\exp\left(-\frac{ic_1r^2}{w_0^2}\right)\exp\left\{i\frac{[\beta_1r\cos(\theta)+\beta_2r\sin(\theta)]}{w_0}\right\}\times\exp[i\varphi(r,\theta)]Q(r,\theta), \tag{11}$$

where A_0 is a constant term, w_0 is the initial beam width, a is the distribution factor parameter, r_0 represents the radius of the primary butterfly ring, $r=\sqrt{x^2+y^2}$, c_1 is the second-order chirp factor, β_1 and β_2 are the initial transverse velocities in the x and y directions, and the phase $\varphi(r,\theta)$ is used to adjust the position of the vortex and the number of topological charges, which can be expressed as

$$\varphi(r,\theta)=l\theta+\alpha r, r>r_1 \tag{12}$$

where l is the vortex topological charge and r_1 is the closest position where the vortex exists. $Q(r,\theta)$ is an aperture that limits the range and energy of the field, and it can be written as

$$Q(r,\theta)=\begin{cases}1, & 0\leqslant r\leqslant R, 0\leqslant\theta\leqslant 2\pi\\ 0, & \text{other}\end{cases} \tag{13}$$

where R is the radius of the outermost ring. In this paper, we use original coordinates that are not normalized to specify

the parameters. We assume that $\lambda = 633$ pm, $q = 1$, $w_0 = 10$ nm, $\alpha = 2\pi$, $r_1 = 200$ nm, $A_0 = 1$, $\beta_1 = \beta_2 = 0$, $c_1 = 0.001$ unless otherwise specified. For magnetic flux density B, we use the international system of units. Substituting Eq. (11) into Eq. (7), we get

$$\psi = \frac{w}{2\pi i}\iint_{\mathrm{R}^2} \rho\psi_0(\rho,\sigma) \times e^{iv\rho^2 - i[S_1\rho\cos(\sigma)+S_2\rho\sin(\sigma)]} d\rho d\sigma. \tag{14}$$

We expand the $Q(r,\theta)$ into a finite sum of complex Gaussian functions, and get $Q(r) = \sum_{j=1}^{N} B_j \exp(-\frac{C_j^2 r^2}{R^2})$, where B_j and C_j are the coefficients and N is the number of complex Gaussian terms [34]. For $\beta_1 = \beta_2 = 0$, $r_1 = 0$, Eq. (14) can be expressed as

$$\psi = \frac{2w}{i}\exp(-il\varphi_2)\exp\left(-a^2\frac{r_0^2}{w_0^2}\right)\sum_{j=1}^{N} B_j \times \sum_{k=0}^{\infty}\frac{\Gamma\left[\frac{1}{2}(l+k)+1\right]}{FE^{\frac{1}{2}(k+1)}\Gamma(l+1)}\exp\left(-\frac{F^2}{8E}\right) \times M_{\frac{1}{2}(k+1),\frac{1}{2}l}\left(\frac{F^2}{4E}\right)\mathrm{Bu}_2\left(0, q\frac{r_0}{w_0}, 0, 0, k\right), \tag{15}$$

where k is odd or zero, Γ is the Gamma function, M is the Whittaker function, $\varphi_2 = \arctan(\frac{S_1}{S_2})$, $E = \frac{a^2}{w_0^2} + \frac{C_j}{R^2} + \frac{ic_1}{w_0^2} - i\frac{B}{4}\cot(\frac{B\tau}{2})$, $F = \sqrt{S_1^2 + S_2^2}$, and

$$\mathrm{Bu}_2(a_1, a_2, a_3, a_4, k) = \int_{-\infty}^{\infty}\frac{\left(2a^2\frac{r_0}{w_0^2} + i\alpha - i\frac{qs^2}{w_0}\right)^k}{k!} \times \exp[i(s^6 + a_4 s^4 + a_3 s^3 + a_2 s^2 + a_1 s)]ds.$$

B. Numerical methods

We utilize the split-step Fourier method to simulate the intensity distribution and the motion trajectory of the ECBVB numerically. Next, we will provide an explanation of how we use this approach. We use a second-order Strang-type splitting scheme which is a method for solving differential equations numerically. The Schrödinger-type operator can be separated into three terms: the diffraction operator L_D, the operator for the parabolic potential L_P, and the operator for the orbital angular momentum L_A. L_A can be divided into two operators, $L_{A,1}$ and $L_{A,2}$, which are proportional to $x\partial y$ and $y\partial x$ respectively. By utilizing the Strang splitting to minimize the number of operations required, we obtain

$$\psi(\tau+\delta) = e^{(L_D+L_P+L_A)\delta}\psi(\tau) = e^{\frac{L_D\delta}{2}}e^{\frac{L_{A,1}\delta}{2}}e^{L_{A,2}\delta}e^{\frac{L_{A,1}\delta}{2}}e^{L_P\delta}e^{\frac{L_D\delta}{2}}\psi(\tau) + O(\delta^3). \tag{16}$$

The diffraction operator can be solved through the utilization of Fourier transforms and inverse Fourier transforms:

$$e^{L_D\delta}\psi = F^{-1}\left\{e^{-i(k_x^2+k_y^2)\delta/2}F\{\psi\}\right\}. \tag{17}$$

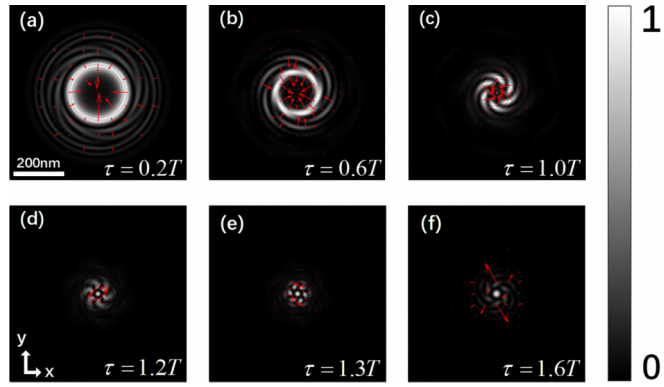

FIG. 1. The normalized intensity distribution (background) and the probability flow density vector (arrows) of the ECBVB propagating in the free space with $w_0 = 10$ nm and $l = 6$.

The parabolic potential which results in a parabolic phase is given by

$$e^{L_P\delta} = e^{-iB^2(x^2+y^2)\delta/16}. \tag{18}$$

By performing the Fourier transformation and the inverse Fourier transformation separately along the y and x axes, one can calculate the integration of $L_{A,1}$ and $L_{A,2}$, and the specific transformation operation can be expressed as

$$e^{L_{A,1}\delta}\psi = F_y^{-1}\{e^{-iBxk_y\delta/2}F_y\{\psi\}\},$$
$$e^{L_{A,2}\delta}\psi = F_x^{-1}\{e^{-iByk_x\delta/2}F_x\{\psi\}\}. \tag{19}$$

III. NUMERICAL SIMULATION AND DISCUSSIONS

A. Free space propagation

1. The probability flow density vectors of the ECBVB

From Fig. 1, we can observe that the probability flow density vector (the arrows) at the initial propagation is inward. The intensity distribution of the ECBVB shrinks inward and its shape becomes smaller gradually. However, once the sidelobes reverse their directions, the directions of the probability density flow will change to be outward. In other words, the directions of the probability flow density vector clearly reveal how the rotation directions of the ECBVB's sidelobes are flipped. The directions of the probability flow density vector on the main lobe or sidelobes are centrosymmetric in arbitrary profile, so it can be verified that the probability density distribution of the ECBVB is centrosymmetric during the propagation process when $l = 6$.

2. Propagation of the ECBVB

The intensity profile of the ECBVB during its propagation in a vacuum is illustrated in Fig. 2, and the white curve represents the corresponding distribution of intensity. It is important to note that the unit of measurement employed in this context is time. In the free space part, we set the value of T corresponding to the case where $B = 5$.

In a vacuum, the ECBVB does not exhibit circular motion like in the presence of the magnetic field due to the absence of any force acting upon it from the magnetic field. The results depicted in Fig. 2 demonstrate that there will be sidelobes

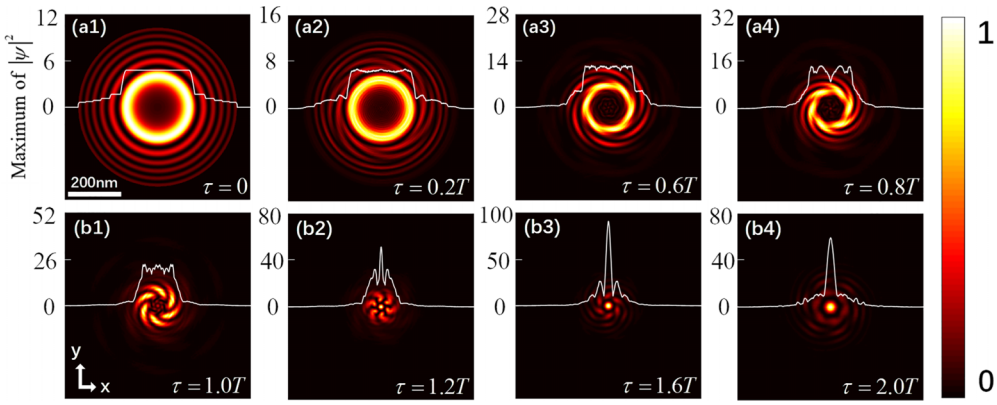

FIG. 2. The normalized intensity distribution of the ECBVB propagating in the free space with $w_0 = 10$ nm, $l = 6$. The white curve is the peak intensity cross-section at different times, and the scale values on the left of the figures are the intensity values corresponding to the white curve.

whose number corresponds to topological charges. We find the intensity distribution is relatively uniform in the main lobe and sidelobes before $0.8T$, and there is little difference in strength between the main lobe and the side lobe. Subsequent to the value of $1.2T$, however, there is an evident gradual concentration of energy towards the center circle, and the intensity difference between the main lobe and the side lobe becomes larger, as shown by the white curve in Fig. 2. The ECBVB begins to autofocus. The rotation directions of the ECBVB's sidelobes are deflected after some moment. Moreover, we find that the position of reversal is related to the focusing position of the ECBVB, so when we appropriately increase or decrease the value of c, the position of reversal is advanced or delayed respectively.

3. Self-healing

In Fig. 3, we observe the change of the electron beam by introducing a Gaussian absorption obstacle and find that the ECBVB has the property of self-healing. We place the Gaussian absorption obstacle at $\tau = 1.20T$, which can be expressed as

$$T(x, y) = 1 - \exp\left[-\frac{(x - G_x)^2 + (y - G_y)^2}{w_G^2}\right], \quad r < r_i, \tag{20}$$

where w_G is the width of the Gaussian absorption obstacle, and r_i is the range in which the Gaussian absorption obstacle exists. We set $(G_x, G_y) = (0, 0)$, then $T(x, y)$ can be written as $T(r) = 1 - \exp[-\frac{r^2}{w_G^2}]$, $r < r_i$.

Figure 3 shows the propagation of an electron beam with different topological charges when the Gaussian absorption obstacle is placed in the $\tau = 1.20T$ plane. In the $\tau = 1.20T$ plane, a circular hole appears in the center of the ECBVB with almost no probability density, which is caused by the Gaussian absorption obstacle. The energy distribution of the ECBVB is mainly concentrated on the main lobes outside the circular hole, and their number depends on the topological charge l; if l is even, then these main lobes are symmetric about the center. Outside each main lobe there is a region with some sidelobes shaped like blades, and the number of blades also depends on the topological charge l. In Fig. 3(c), after the ECBVB passes through the Gaussian absorption obstacle, its intensity distribution focuses again. After that, the circular hole-shaped defect area quickly heals, which means that the energy outside the hole flows to the defect area. However, the healing pattern expands outside from the center of the hole gradually, so the energy does not flow inside from the outside of the defect area directly. After the ECBVB heals, not only the main lobes whose amount depends on topological charges diffuse inward but also several rings of different sizes appear in the central area of the original circular hole surrounded by these main lobes. By observation, we find that the greater the topological charge l is, the more rings there are, as shown in Figs. 3(b1)–3(b3).

Moreover, we discover that changing the size of the Gaussian absorption obstacle affects the self-healing properties of the ECBVB. When we increase the range r_i of the Gaussian absorption obstacle, the peak intensity of the ECBVB after passing through the Gaussian absorption obstacle becomes lower. By comparing Figs. 4(a1)–4(a3), we find that the healing pattern at the center of the ECBVB passing through the Gaussian absorption obstacle is smaller when the corresponding value of r_i is larger, which can be reflected in Figs. 4(a2) and 4(a3), and the conical beam behind the Gaussian absorption obstacle becomes thinner. In particular, Fig. 4(a3) reveals that when we increase the value to a certain extent, the phenomenon of secondary autofocusing disappears. Figure 4(b) is the peak intensity diagram during the propagation process of the ECBVB under different r_i; the larger the value of r_i, the lower the intensity of the ECBVB after passing the Gaussian absorption obstacle. Combined with Fig. 4, it can be inferred that the self-healing performance of the ECBVB is not significantly correlated with the focused conical beam in the middle before the Gaussian absorption obstacle but is closely related to the area around the conical beam.

In addition, after adding the Gaussian absorption obstacle, the ECBVB forms an EB when $r_i = 40$ nm. As shown in Fig. 4(a1) where the white coil is placed, there is a dark area in the middle, and the first focus of the ECBVB forms the head of the EB. Then the ECBVB partially diverges to the sides, forming the main body of the EB. Finally, the ECBVB focuses again to form the bottom of the EB. This property is expected to be applied to trapping particles.

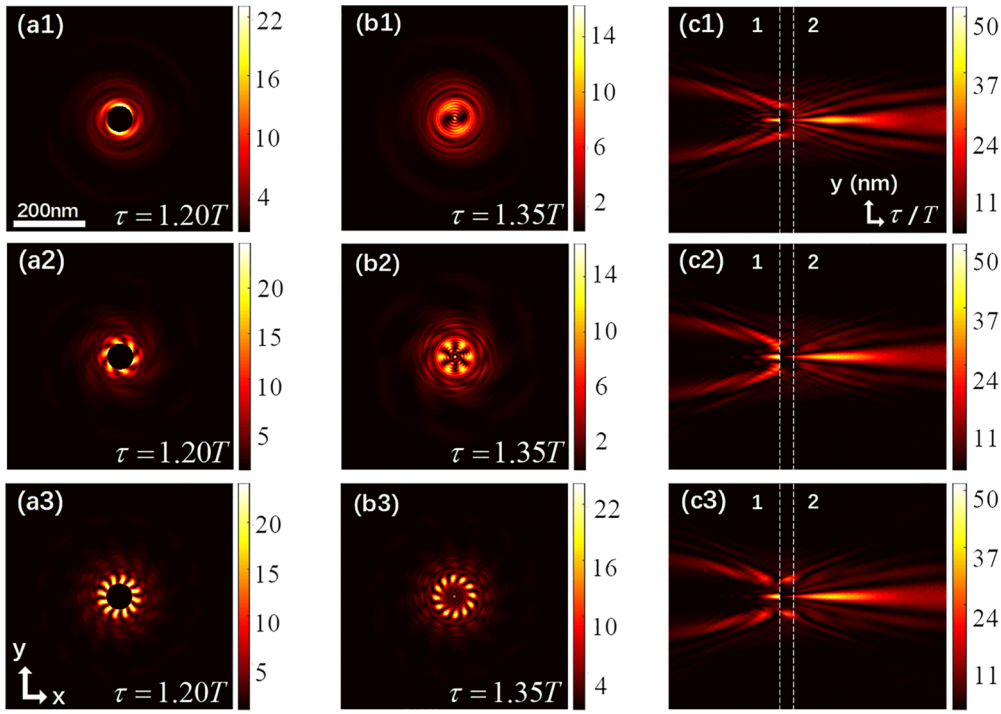

FIG. 3. Propagation of the ECBVB with $w_0 = 10$ nm, $r_i = 40$ nm under different values of l. (a1)–(a3) $\tau = 1.20T$ plane. (b1)–(b3) $\tau = 1.35T$ plane. (c1)–(c3) Side views of the ECBVB propagating with $l = 2, 6, 12$. Panels (a) and (b) correspond to planes 1 and 2 marked in panel (c), respectively.

B. Constant magnetic-field propagation

1. Propagation of the ECBVB

Figure 5 shows the intensity of the ECBVB change over a cycle, from which we can get some of its dynamic characteristics. We can see that the initial plane appears toroidal. In the process that follows, the ECBVB gradually contracts inward, and some sidelobes appear on the outside of the inner ring. At $\tau = T/2$, the ECBVB shrinks into a tiny fraction, at which moment its intensity becomes extremely large. After $\tau = T/2$, the ECBVB diffuses outward again. An interesting phenomenon of the external vortex is that the sidelobes outside the inner rings of the ECBVB reverse directions after $\tau = T/2$. It must be emphasized that the sidelobes and the interior of the main lobe rotate dynamically during propagation. At the beginning of propagation, the rotation speed inside the main lobe increases to a high level gradually in half a cycle, and then gradually decreases after half a cycle, until one cycle when the rotation is exactly no longer. During the whole process, we observe that the interior of the ECBVB rotates counterclockwise at high speed because of the action of the vortex. At $\tau = T/8$, the sidelobes rotate clockwise as shown in Fig. 5(a2), then the overall shape of the ECBVB gradually becomes smaller. At $\tau = 3T/8$, the rotation directions of the sidelobes change from clockwise to counterclockwise due to internal rotation and the constant magnetic field. After $\tau = T/2$, the sidelobes turn clockwise again, and the shape of the ECBVB gradually expands and returns to the original state.

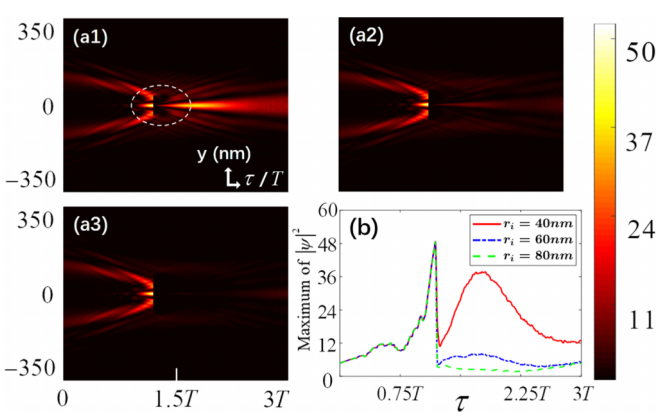

FIG. 4. Propagation of the ECBVB with $w_0 = 10$ nm, $l = 6$ under different values of r_i. (a1)–(a3) Side views of the ECBVB propagating with $r_i = 40, 60,$ and 80 nm. (b) Peak intensity as a function of the propagation time τ for different values of r_i, and the three curves correspond to panels (a1), (a2), and (a3) respectively.

2. Initial transverse velocity

There is a linear phase $[\beta_1 r\cos(\theta) + \beta_2 r\sin(\theta)]/w_0$, which produces an initial transverse velocity $\binom{\beta_1}{\beta_2}$. The motion caused only by the initial velocity is a circular trajectory with radius $R = \frac{\sqrt{\beta_1^2+\beta_2^2}}{B}$.

In Fig. 6, it is found that the central area of the electron beam is obviously moved, and the pattern of the ECBVB gradually moves away from the origin of the coordinates. The center of the ECBVB successively moves to the right up, right down, left down, and finally slowly returns to the center of the coordinate. During the whole process, the rotating motion and the pattern of the ECBVB are not altered by the linear phase.

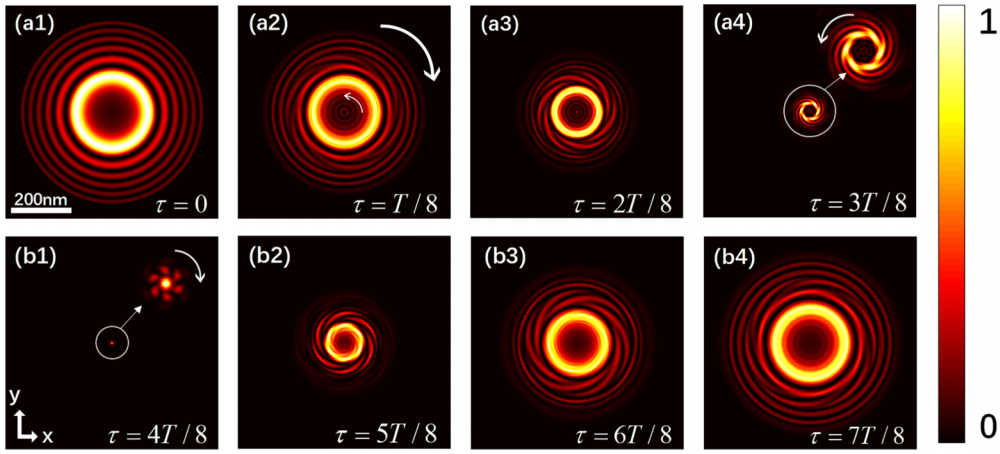

FIG. 5. The normalized intensity distribution during a cycle of the ECBVB propagating in the constant magnetic field with $w_0 = 10$ nm, $l = 6$, $B = 5$. The white arrows represent the direction of rotation of the sidelobes and within the main lobe.

3. The influence of magnetic flux density B and initial beam width w_0

To further investigate the autofocusing characteristics of the ECBVB, we look for the influence of different parameters on the autofocusing distance and the autofocusing intensity of the ECBVB. Different magnetic flux densities will lead to different cycles. When approaching the end of a cycle, the intensity of the ECBVB is very small compared with the peak intensity, so the cycle corresponding to $B = 6$ is adopted in the Fig. 7(a). A valuable phenomenon is that magnetic flux intensity influences the maximum focus intensity and the focus position. As shown in Fig. 7, the ECBVB will reach a relative maximum value before focusing, and the position of the relative maximum value is close to the position of the absolute maximum focusing intensity. We find a positive correlation between the maximum autofocusing intensity and the magnetic flux density: with the increase of the magnetic-field intensity, the maximum autofocusing intensity and the autofocusing distance of the ECBVB also increase. However, an increase in autofocusing intensity also means that the energy of the ECBVB is more concentrated, which leads to a decrease in the focal depth. It is seen from Fig. 7(a) that the higher the crest of the bulge is, the narrower the crest is. To better observe the change of the focal depth, we use normalized intensity instead of peak intensity in Figs. 7(b1)–7(b5). For the case of different magnetic flux intensities, the ECBVB achieves autofocusing and has a relative maximum value before focusing, and the depth of the relative maximum peak is close to the focal depth. Two depths have the same variation trend when magnetic flux intensity changes.

When the magnetic-field intensity is small, the wave crest is relatively flat, and the focal depth is larger. However, with the increase of the magnetic-field intensity, the wave crest gradually becomes sharp, and the focal depth becomes smaller. We find in Fig. 7(a) that when the magnetic-field intensity increases, the relative maximum intensity and the absolute maximum focusing intensity increase concurrently. However, in Figs. 7(b1)–7(b5), due to the use of the normalized intensity, the maximum intensity of the ECBVB in one cycle is 1. With the increase of the magnetic-field intensity, the relative maximum gradually decreases, which means that the relative difference value between the relative maximum and the absolute maximum intensity also increases. Moreover, we note that with the initial beam width w_0 increasing, the focusing intensity of the ECBVB also increases with little change in the corresponding depth of focus. Different from the case of increasing the strength of the constant magnetic field, increasing the value of w_0 appropriately causes the relative difference between the relative maximum and the absolute maximum intensity of the ECBVB to decrease.

4. The influence of vortex

Contrary to the situation in Ref. [19], the focusing intensity of the ECBVB decreases when the vortex exists. This is because the vortices contribute to the production of sidelobes whose number is equivalent to the topological charges. As a result, the partial energy originally concentrated in the center is divided equally among these sidelobes, as shown in Fig. 8(b). Interestingly, the topological charges have almost no effect on the peak intensity of the ECBVB, which is related

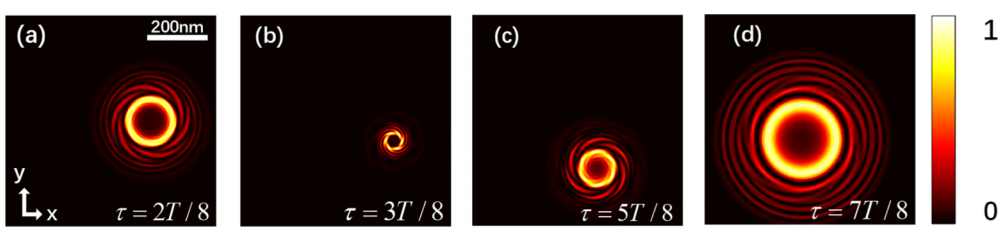

FIG. 6. The normalized intensity distribution of the ECBVB propagating in the constant magnetic field with $w_0 = 10$ nm, $l = 6$, $B = 5$, and $\beta_1 = \beta_2 = 5$. We build the coordinates from the center of the figures.

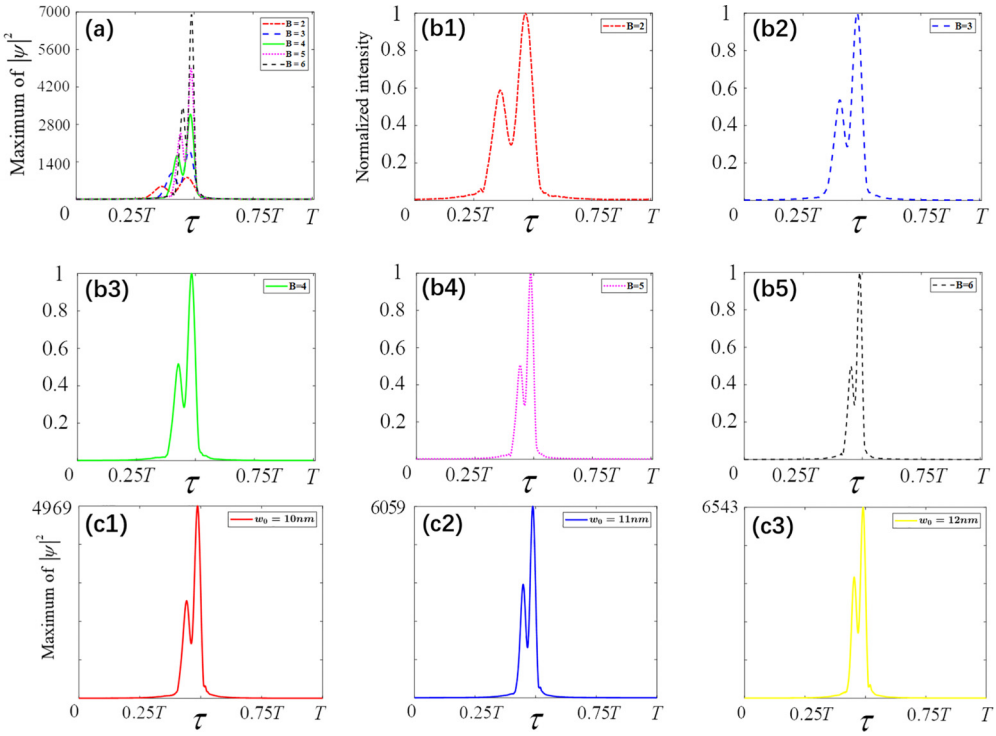

FIG. 7. The peak intensity and the normalized intensity of the ECBVB propagating in the constant magnetic field with different parameters when $l = 6$. (a), (b1)–(b5) With different B. (c1–c3) With different w_0 when $B = 5$.

to the range in which we set the vortex. Although changing the topological charges causes a change in the number of sidelobes, when a given vortex is present, the intensity of the central circle which determines the peak intensity remains constant. In other words, the energy assignment relationship of the central circle is fixed for different values of l when the vortex exists.

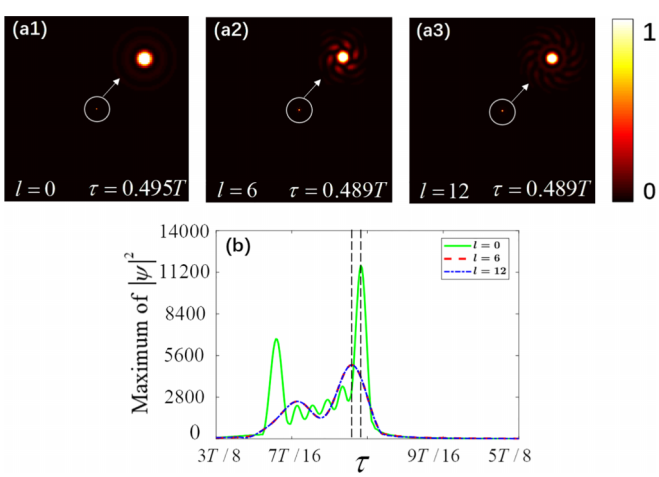

FIG. 8. The normalized cross-section intensity distribution and the peak intensity of the ECBVB with and without vortex when $w_0 = 10$ nm, $B = 5$. (a1)–(a3) Snapshots of the normalized cross-section intensity distribution of the ECBVB at the plane marked in (b). (b) The peak intensity of the ECBVB with different l.

5. The influence of the second-order chirp parameter

In order to adjust the focusing effect and the focusing position of the electron beam, we set a second-order chirp factor c_1 in the initial field of the ECBVB, as shown in Fig. 9. When $c_1 = 0.001$, the ECBVB achieves the autofocusing in one cycle, and the autofocusing time is relatively short, as shown by the red line in Fig. 9(a). In this case of $c_1 > 0$, we gradually increase the value of c_1 and find that the focusing position of the ECBVB is gradually pushed forward, the maximum focusing intensity of the ECBVB increases, and the

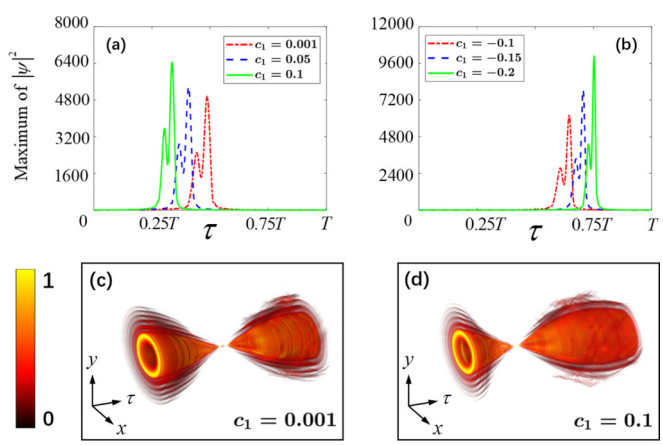

FIG. 9. The peak intensity and the three-dimensional normalized intensity distribution of the ECBVB propagating in a constant magnetic field with different second-order chirp parameters when $w_0 = 10$ nm, $l = 6$, $B = 5$.

focus depth of the ECBVB is almost unchanged. In Figs. 9(c) and 9(d), we can see that the peak intensity (when the pattern size is minimal) of the ECBVB corresponds to different times when the value of c_1 is different. If we want to adjust the focusing position of the ECBVB backward, we can make the second-order chirp factor negative. For example, when $c_1 = -0.15$, the focusing position of the ECBVB shifts backward obviously and the ECBVB still maintains the autofocusing in one cycle. When c_1 is negative, increasing the absolute value of c_1 still increases the maximum focusing intensity of the ECBVB. By adjusting the second-order chirp factor, we find that the focal intensity changes along with the change in the focal position. If we want to precisely achieve the desired value for the intensity at the focal position, we only need to add a proportional coefficient to the initial field. However, this will increase the complexity and cost of practical applications. If the initial beam width is adjusted together with the second-order chirp factor mentioned above, it is possible to set the focal length and the focusing intensity we want without changing the depth of focus.

IV. CONCLUSION

In summary, we propose the ECBVB based on the butterfly catastrophe and numerically investigate the propagation properties of the ECBVB in free space and a constant magnetic field. In free space, we discuss the cross-section intensity distribution and autofocusing property of the ECBVB. Then, the inversion of the sidelobes is revealed by the variation of the probability density flow. After introducing a Gaussian absorption obstacle, we discuss how the ECBVB achieves self-healing, the influence of the radius of the Gaussian absorption obstacle on its self-healing performance, and the generation of the EB. In a constant magnetic field, the rotation behavior of the ECBVB is investigated, and we find that the initial transverse velocity determines the monolithic rotation radius of the ECBVB. The focusing intensity of the ECBVB in a magnetic field is two orders of magnitude higher than that in free space. Moreover, the autofocusing property of the ECBVB exhibits flexible tunability. The focal length, the focal depth, and the focusing intensity of the ECBVB can be adjusted by altering the distribution factor, the magnetic flux density, and the second-order chirp factor. These properties have potential application prospects in the microetch process and particle capture.

ACKNOWLEDGMENTS

The authors acknowledge support from National Natural Science Foundation of China (Grants No. 12174122 and No. 11775083), Guangdong Provincial Natural Science Foundation of China (Grant No. 2022A1515011482), and Program of Innovation and Entrepreneurship for Undergraduates (Grant No. S202310574145). Special Funds for the Cultivation of Guangdong College Students' Scientific and Technological Innovation ("Climbing Program" Special Funds) (pdjh2024b124).

[1] J. Pierce, J. Webster, H. Larocque, E. Karimi, B. McMorran, and A. Forbes, Coiling free electron matter waves, New J. Phys. **21**, 043018 (2019).

[2] V. Grillo, G. C. Gazzadi, E. Mafakheri, S. Frabboni, E. Karimi, and R. W. Boyd, Holographic generation of highly twisted electron beams, Phys. Rev. Lett. **114**, 034801 (2015).

[3] A. Forbes, M. de Oliveira, and M. R. Dennis, Structured light, Nat. Photon. **15**, 253 (2021).

[4] R. Shiloh, Y. Lereah, Y. Lilach, and A. Arie, Sculpturing the electron wave function using nanoscale phase masks, Ultramicroscopy **144**, 26 (2014).

[5] K. Y. Bliokh, Y. P. Bliokh, S. Savel'ev, and F. Nori, Semiclassical dynamics of electron wave packet states with phase vortices, Phys. Rev. Lett. **99**, 190404 (2007).

[6] M. Uchida and A. Tonomura, Generation of electron beams carrying orbital angular momentum, Nature (London) **464**, 737 (2010).

[7] J. Verbeeck, H. Tian, and P. Schattschneider, Production and application of electron vortex beams, Nature (London) **467**, 301 (2010).

[8] B. McMorran, A. Agrawal, I. Anderson, A. Herzing, H. Lezec, J. Mcclelland, and J. Unguris, Electron vortex beams with high quanta of orbital angular momentum, Science **331**, 192 (2011).

[9] V. Grillo, G. Carlo Gazzadi, E. Karimi, E. Mafakheri, R. W. Boyd, and S. Frabboni, Highly efficient electron vortex beams generated by nanofabricated phase holograms, Appl. Phys. Lett. **104**, 043109 (2014).

[10] G. Pozzi, P.-H. Lu, A. H. Tavabi, M. Duchamp, and R. E. Dunin-Borkowski, Generation of electron vortex beams using line charges *via* the electrostatic Aharonov-Bohm effect, Ultramicroscopy **181**, 191 (2017).

[11] S. M. Lloyd, M. Babiker, G. Thirunavukkarasu, and J. Yuan, Electron vortices: Beams with orbital angular momentum, Rev. Mod. Phys. **89**, 035004 (2017).

[12] K. Y. Bliokh *et al.*, Theory and applications of free-electron vortex states, Phys. Rep. **690**, 1 (2017).

[13] N. Voloch-Bloch, Y. Lereah, Y. Lilach, A. Gover, and A. Arie, Generation of electron Airy beams, Nature (London) **494**, 331 (2013).

[14] D. V. Karlovets, Gaussian and Airy wave packets of massive particles with orbital angular momentum, Phys. Rev. A **91**, 013847 (2015).

[15] D. V. Karlovets, Scattering of wave packets with phases, J. High Energ. Phys. 03 (2017) 049.

[16] D. Grosman, N. Sheremet, I. Pavlov, and D. Karlovets, Elastic scattering of Airy electron packets on atoms, Phys. Rev. A **107**, 062819 (2023).

[17] V. Grillo, E. Karimi, G. C. Gazzadi, S. Frabboni, M. R. Dennis, and R. W. Boyd, Generation of nondiffracting electron Bessel beams, Phys. Rev. X **4**, 011013 (2014).

[18] V. Grillo, J. Harris, G. C. Gazzadi, R. Balboni, E. Mafakheri, M. R. Dennis, S. Frabboni, R. W. Boyd, and E. Karimi, Generation and application of Bessel beams in electron microscopy, Ultramicroscopy **166**, 48 (2016).

[19] S. Hettler, L. Grünewald, and M. Malac, Quasi non-diffractive electron Bessel beams using direct phase masks with applications in electron microscopy, New J. Phys. **21**, 033007 (2019).

[20] B. Thaller, *Visual Quantum Mechanics* (Springer, New York, 2000).

[21] L. D. Landau and E. M. Lifshitz, *Quantum Mechanics: Non-Relativistic Theory* (Elsevier, Amsterdam, 2013).

[22] M. Goutsoulas and N. K. Efremidis, Dynamics of self-accelerating electron beams in a homogeneous magnetic field, Phys. Rev. A **103**, 013519 (2021).

[23] H. Tang, Z. Fan, S. Ouyang, Z. Mo, D. Xu, H. Huang, and D. Deng, Airy transform of an electron Landau state in a longitudinal constant magnetic field, Results Phys. **50**, 106552 (2023).

[24] H. Huang, H. Tang, X. He, Y. Wu, X. Cai, X. Deng, and D. Deng, Electron symmetric pearcey Gaussian vortex beams, Ann. Phys. (NY) **534**, 2200202 (2022).

[25] X. He, H. Huang, C. Xu, X. Deng, Y. Wu, H. Tang, D. Xu, S. Luo, J. Liu, R. Wu, and D. Deng, Dynamics of electron Pearcey Gaussian beams in a constant magnetic field, Ann. Phys. (NY) **534**, 2200238 (2022).

[26] M. Mutzafi, I. Kaminer, G. Harari, and M. Segev, Non-diffracting multi-electron vortex beams balancing their electron-electron interactions, Nat. Commun. **8**, 650 (2017).

[27] A. Jesacher, S. Füurhapter, S. Bernet, and M. Ritsch-Marte, Shadow effects in spiral phase contrast microscopy, Phys. Rev. Lett. **94**, 233902 (2005).

[28] R. Juchtmans, A. Béché, A. Abakumov, M. Batuk, and J. Verbeeck, Using electron vortex beams to determine chirality of crystals in transmission electron microscopy, Phys. Rev. B **91**, 094112 (2015).

[29] E. C. Zeeman, Catastrophe theory, in *Structural Stability in Physics* (Springer-Verlag, Berlin, 1979), pp. 12–22.

[30] M. V. Berry and C. J. Howls, Axial and focal-plane diffraction catastrophe integrals, J. Phys. A **43**, 375206 (2010).

[31] V. I. Arnol'd, Critical points of smooth functions and their normal forms, Russ. Math. Surv. **30**, 1 (1975).

[32] Y. Cai, J. Hu, Z. Sun, Y. Lan, T. Houan, and Y. Qian, Manipulation and improvement of autofocusing properties for circular butterfly beams, Ann. Phys. (NY) **534**, 2200235 (2022).

[33] Q. Wei, J. Jiang, Z. Mo, D. Xu, X. Cai, Z. Liang, J. Shi, H. Huang, and D. Deng, Symmetric swallowtail beams in the rectangle frame, Ann. Phys. (NY) **535**, 2200466 (2023).

[34] D. Deng, J. Li, and Q. Guo, Propagation of truncated modified Laguerre–Gaussian beams, Appl. Phys. B **98**, 211 (2010).